

Contents lists available at ScienceDirect

Petroleum Science

journal homepage: www.keaipublishing.com/en/journals/petroleum-science



Original Paper

High-resolution coupling of stratigraphic 'sweet-spot' lithofacies and petrophysical properties: A multiscale study of Ordovician Goldwyer Formation, Western Australia



Yu-Jie Yuan ^{a, b, h, *}, Reza Rezaee ^b, Jian-Wei Gu ^c, Song-Tao Wu ^{d, e}, Emad A. Al-Khdheeawi ^{b, f}, Jun Wang ^a, Bin Pan ^g

- ^a School of Earth Sciences, Yunnan University, Kunming, Yunnan, 650500, China
- ^b Western Australian School of Mines: Minerals, Energy and Chemical Engineering, Curtin University, Perth, Western Australia, Australia
- ^c School of Petroleum Engineering, China University of Petroleum (East China), Qingdao, Shandong, 266580, China
- ^d Research Institute of Petroleum Exploration and Development, CNPC, Beijing, 100083, China
- ^e National Energy of Tight Oil and Gas R&D Center, Beijing, 100083, China
- f Petroleum Technology Department, University of Technology-Iraq, Baghdad, 10066, Iraq
- g School of Civil and Resource Engineering, University of Science and Technology Beijing, No. 30, Xueyuan Road, Beijing, 10083, China
- h State Key Laboratory of Coal Mine Disaster Dynamics and Control, Chongqing University, Chongqing, 400044, China

ARTICLE INFO

Article history: Received 18 March 2022 Received in revised form 17 August 2022 Accepted 1 November 2022 Available online 10 November 2022

Edited by Teng Zhu and Jia-Jia Fei

Keywords: Shale Nanopore structure Pore characterization Lithofacies

ABSTRACT

The identification of stratigraphic 'sweet-spot' interval is significant in oil and gas formation evaluation. However, formation evaluation in macroscopic-scale merely provides low resolution and limited information, thus may lead to uncertainties in resource estimation. To accurately identify the 'sweet-spot' intervals amongst heterogeneous lithofacies, we conducted a very high-resolution and quantitative analysis from in-situ macroscopic scale to laboratory microscopic scale on the Goldwyer formation of Canning Basin, Western Australia. The comprehensive advanced well logging and slim-compact micro imager (SCMI) technologies were synthetically applied in couple with the laboratory nanoscaled experiments. The results unveiled an extraordinarily large lithofacies heterogeneity between different rock intervals, with distinguished features shown in Goldwyer I, II, and III members. The most favorable lithofacies is recognized as the laminated argillaceous thermally-matured organic matter (OM)-rich mudstone, which is widely developed in Goldwyer III as the major attributor to 'sweet-spot' intervals. Goldwyer III is exclusively characterized by thick mudstone intervals (94.4%), interbedded with thin calcareous mudstones (5.5%), corresponding to a depositional environment of low-energy distal section of the outer ramp settings. Microscopically, the most favorable lithofacies in 'sweet-spot' intervals develop numerous OM-/mineral nanopores for hydrocarbon storage. Illite-rich lithofacies develops abundant inter-particle pores from 2 to 17 nm that mainly contribute to pore volume for free gas storage capacity. OM-rich lithofacies with higher maturity have OM-pores with good connectivity, bearing large specific surface area that is beneficial for adsorbed gas capacity.

© 2022 The Authors. Publishing services by Elsevier B.V. on behalf of KeAi Communications Co. Ltd. This is an open access article under the CC BY-NC-ND license (http://creativecommons.org/licenses/by-nc-nd/4.0/).

1. Introduction

The global demand for energy supply urgently requires the unconventional gas resource from a long-term perspective. Shale,

E-mail address: yujieyuan@ynu.edu.cn (Y.-J. Yuan).

as one of the most potential unconventional resources, is a laminated fine-grained sedimentary rock that has a high vertical heterogeneity in mineralogical, petrological and petrophysical properties (Luffel et al., 1992; Passey et al., 2010; Rezaee, 2015). The high degree of heterogeneity is closely associated with lithofacies (Lazar et al., 2015) that was originally utilized as the lithological properties of sedimentary rocks (Eberzin, 1940), followed by a description of the fundamental rock unit generated in a sedimentary depositional environment (Krumbein, 1948; Slatt et al., 2014).

^{*} Corresponding author. School of Earth Sciences, Yunnan University, Kunming, 650500, China.

Lithofacies description involves a comprehensive understanding of lithological features from both qualitative and quantitative perspectives, e.g., mineralogical, geochemical, texture, structure, stratification, colour, clast roundness and sorting, and hydrocarbon potential properties (Slatt and Rodriguez, 2012; Liu et al., 2019a; Zhang et al., 2020). The ratio of clastic and sand-shale components was also used to be generally applied in lithofacies mapping and the establishment of 3D lithofacies model (Sloss, 1950; Walker, 1962; Wang and Carr, 2012). Among all those parameters, lithofacies of shale is much more influenced by mineralogical and organic matter (OM) richness than rock stratification and internal structures. As per mineralogical composition (e.g., clay, quartz, carbonate), shale lithofacies are classified into: (i) argillaceous lithofacies (AR type, that is abundant with clay contents), (ii) siliceous lithofacies (SI type, that is abundant with quartz), (iii) calcareous lithofacies (CA type, that is abundant with carbonates) and (iv) mixed lithofacies, following the nomenclature scheme proposed by Lazar et al. (2015). OM richness, quantified by total organic carbon (TOC) content, is synthetically applied in couple with mineral compositions as the most significant factors for the identification of lithofacies. In this regard, 12 lithofacies are identified for Goldwyer Formation in Canning Basin, Western Australia (WA). Further investigations revealed the influence of lithofacies on shale nanopore structure that is intimated with shale gas storage capacity (Yuan et al., 2021a).

Shale storage capacity is highly dependent on nanopore structure that can be characterized by pore type, pore shape, porosity, pore size distribution (PSD), pore volume (PV), specific surface area (SSA), fractal dimension and pore connectivity (Zou et al., 2013; Hu et al., 2015; Ge et al., 2016; Jiang et al., 2016; Yang et al., 2016; Sun et al., 2019; Yuan and Rezaee, 2019a, b). Pore types were categorized into: (i) mineral-related pores, e.g., inter-particle (Inter-P) and intra-particle (Intra-P) pores, and (ii) organic matter (OM) pores (Loucks et al., 2010). Inter-P pores are developed between mineral particles/grains or crystals, including quartz, clay, feldspar and carbonates. The pore diameter of Inter-P pores presents to be larger and universally exhibits the shape from elongate to angular. Intra-P pores are developed within particles with a large variation of pore sizes and poor connectivity. OM pores within different types of OM can demonstrate various pore diameters as thermal maturity increases (Chen and Xiao, 2014; Liu et al., 2019b; Wu et al., 2019; Gao et al., 2020). With regard to pore size, the standard of International Union of Pure and Applied Chemistry is commonly applied in pore systems of shale. Micropores, mesopores and macropores (defined by the pore sizes less than 2 nm, from 2 to 50 nm, and larger than 50 nm, respectively (Rouquerol et al., 1994)) are associated with various pore types developed within minerals and OM that constitute a high degree of lithofacies heterogeneity in different depth of the same shale formation (Curtis et al., 2012; Xu et al., 2021).

The stratigraphic 'sweet-spot' interval is the most prospective reservoir interval for commercial success of shale gas; it is thus significant to distinguish the most favorable lithofacies for 'sweet-spot' identification (Loucks and Ruppel, 2007; Liu et al., 2019a; Guan et al., 2021). However, lithofacies identification is challenging in shale formation compared to the conventional sandstone or carbonates, owing to the large heterogeneity from macro-to microscope scale. The scale of lithofacies description is categorized into region scale, well scale and core scale (Coates et al., 1999; Wang and Carr, 2012; Xiao et al., 2015). The larger scaled investigations have been well-established, whereas the coupling relationship between different scales remains unclear and questionable. How to upscale the discrete core scale data into a larger and continuous well scale in a high-resolution is a challenge to deal with (Yuan, 2020; Cai et al., 2022). Furthermore, the identification of

stratigraphic 'sweet-spot' intervals in Goldwyer Formation, WA, remains unclear; thus more details are required to be clarified.

In this study, multiscale analysis was carried out in a high resolution from micro- to macroscopic scope. The advanced logging interpretations are integrated with the results of laboratory core analysis, on purpose to (1) elucidate the depositional environment of different Goldwyer members, (2) identify the stratigraphic 'sweet-spot' intervals, (3) determine the favourable lithologies and lithofacies of the stratigraphic 'sweet-spot' intervals, and (4) to analyze nanopore structures of the stratigraphic 'sweet-spot' intervals. A coupling relationship between the favorable lithofacies of stratigraphic 'sweet-spot' intervals and the nanopore attributes (i.e., pore type, pore shape, PSD, PV, and SSA) is revealed.

2. Geological settings

Geographically, Canning Basin is situated in the north western part of WA (Fig. 1). Constructed by structural regions that are trending in NW–SE direction, Canning Basin covers a total area of ~506,000 km², among which the onshore section occupying ~430,000 km², and constitutes the largest sedimentary basin in WA (Brown et al., 1984; Kennard et al., 1994; Geoscience Australia, 2007). The sediment thickness was accumulated maximally up to > 15,000 m within the depocentres, which are consisted of (i) the southern trough Palaeozoic depocentre comprising Willara Subbasin and Kidson Sub-basin, and (ii) the northern trough including Fitzroy Trough and the Gregory Sub-basin. Tectonically, as shown in Fig. 1, the central arch depocentre is subdivided into the Broome platform and Crossland platform.

The sedimentary stratigraphic succession of the onshore Canning Basin covers the age of Lower Ordovician (Forman and Wales, 1981) (Fig. 2). The Goldwyer Formation, covering ~124,000 km² of resource prospectivity, containing 70.7 Tm³ gas in-place and a risked recoverable shale gas resource estimated ~3.18 Tm³ (Kuuskraa et al., 2013). The Goldwyer Formation is widely deposited in the southern and central part of the Canning Basin that is potentially abundant in organic matter (Van Hattum et al., 2019), with total organic carbon (TOC) contents ranging up to 6.4% and an average thickness of 350 m. This study therefore targets on the interval of Ordovician Goldwyer Formation, from Theia-1 well located in Broome Platform at the depth of 1188.5-1593.2 m. The whole objective interval was subdivided into three members: Goldwyer I member (1188.5–1366.0 m), Goldwyer II member (1366.0-1472.6 m), and Goldwyer III member (1472.6-1593.2 m), which demonstrate different patterns of compositional and petrophysical properties.

3. Materials and methods

3.1. Shale samples

A set of 22 samples from Goldwyer I, II, and III members via Theia-1 well were studied, taking into consideration of the variability in mineralogical compositions, petrological features and geochemical properties. To reveal the impact of lithofacies on microscopical nanopore structure parameters, we selected twelve samples from Goldwyer I, four samples from Goldwyer II, and six samples from Goldwyer III, for detailed lithofacies investigation.

Among these samples, representative mudstone samples from Goldwyer III were selected for further laboratory petrophysical experiments (e.g., scanning electron microscopy (SEM), low-pressure $\mathrm{CO_2/N_2}$ gas adsorption), to analyze microscopic pore structure parameters (i.e., pore shape, PSD, PV, SSA).

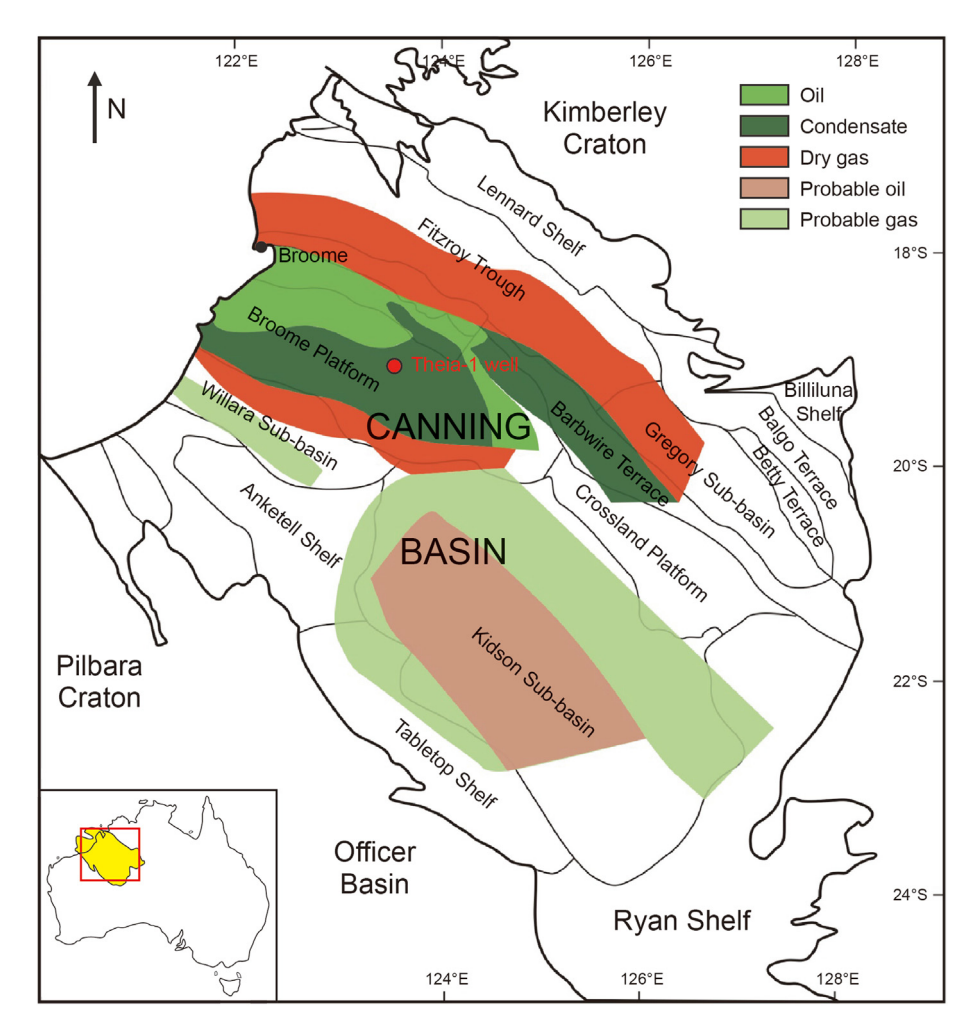


Fig. 1. The map of the Canning Basin in Western Australia and the location of Theia-1 well. The map was adapted from Department of Mines and Petroleum (2014).

3.2. X-ray diffraction (XRD)

The mineralogical compositions of whole-rock and clay-fraction were measured using X-ray diffraction (XRD). Prior to the test, each sample was disaggregated in a mortar and pestle and grounded into the powder less than 200 meshes with the mass of approximately 5 g. To analyze clay diffraction, each sample was processed with H_2O_2 , followed by the dispersing and sedimenting procedures within Calgon (a base liquid). The aliquots were pipetted from the contact layer of sediments and liquid, while the suspension fluid was processed at vacuum on a ceramic tile. Subsequently, the oriented clays were distinguished by employing various conditions.

XRD mineralogical composition analysis was performed using Bruker D8 Advance automated powder diffractometer equipped with a LynxEye sensitive detector and a Cu X-ray tube. The whole rock samples were analyzed over an angular range of $7-120^{\circ}~2\theta$ with a normal step size of 0.015° . The mineral phases were determined utilizing the Bruker EVA software for search/match analysis and a comprehensive full pattern data analysis programme, Bruker TOPAS. The clay mineral aggregates were processed following the procedures proposed by US Geological Survey (Poppe et al., 2001).

3.3. Thin section petrographic analysis

To study the petrological and mineralogical characteristics of the tested samples, thin sections were prepared in a standard size following the procedures as below. (i) Immerse the samples within epoxy to enhance cohesion and avoid the waste of samples during grinding. (ii) Add blue dye to the epoxy to improve the visualization of nanopore structure. (iii) Mount the thinly-sliced samples on a frosted glass slide and then ground to the thickness of ~20 μm . Once thin-section was completed, standard petrographic analysis was conducted using Leica DM6000M Reflected Petrographic microscope apparatus under plain polarized and crossed polarized lighting conditions.

3.4. Scanning electron microscopy (SEM)

Prior to the test, some samples (e.g., samples from Goldwyer III shale interval) were polished with an argon (Ar) ion mill using Leica EM TIC 3X apparatus, on purpose to generate an extraordinarily flat and artifact-free surface that can improve the visualization of nanopores. Other samples (e.g., samples from Goldwyer I and II) were processed to expose the fresh surfaces for field emission-scanning electron microscopy (FE-SEM).

FE-SEM was carried out on each sample for a high magnification imaging, using a FEI Quanta FEG250 scanning electron microscope that was operating at relatively low beam energy (10 kV–15 kV), in a high pressure (~60 Pa) vacuum chamber environment. The secondary electron (SE) and backscattered electron (BSE) images of the samples were collected for pore structure analysis.

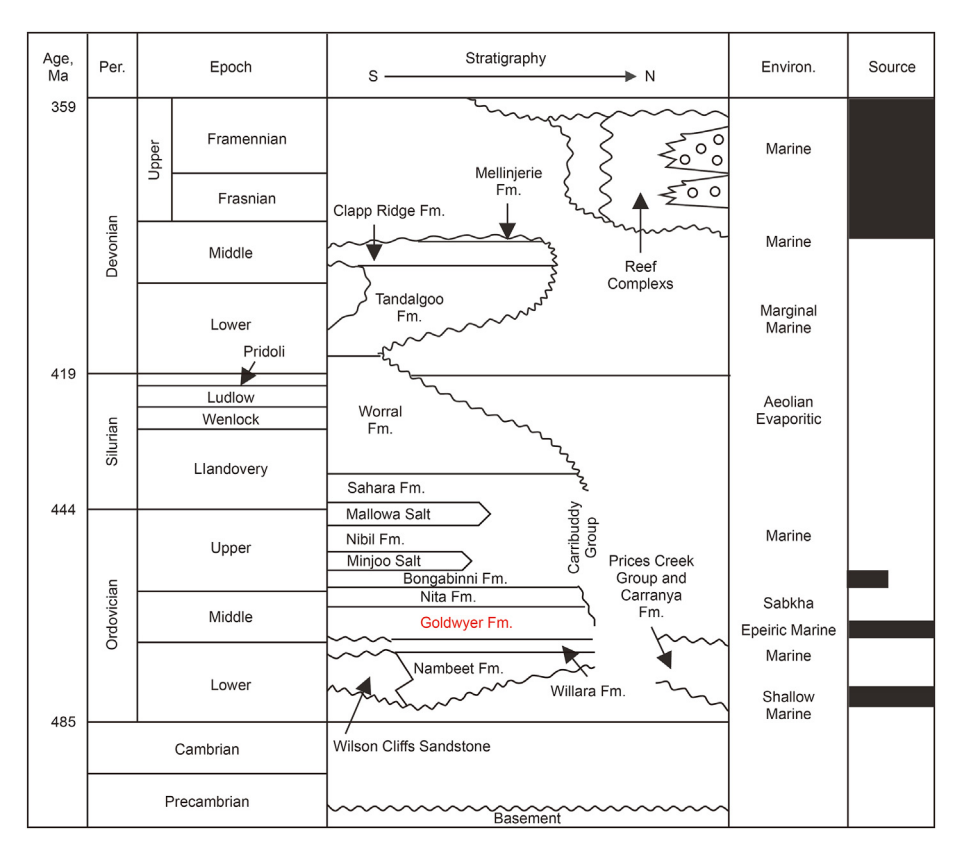


Fig. 2. Stratigraphic column, environment, and the petroleum source of the onshore Canning Basin, Western Australia (adapted from the Department of Mines and Petroleum, 2014).

3.5. Rock-Eval pyrolysis

To analyze organic geochemical attributes in the target interval and compare between three different Goldwyer members, Rock-Eval pyrolysis was carried out on Rock-Eval VI® apparatus. Shale samples were crushed into 60-80 meshes with the mass of 60-80 mg (Lafargue et al., 1998). The whole process of Rock-Eval pyrolysis was a temperature-programmed heating of the crushed sample in an inert atmosphere. Bulk samples were firstly pyrolyzed under inert N2, followed by a burning of residual carbon in an oxidation oven. During the process, S1 peak (units of mg HC/g, the milligram hydrocarbon per gram of rock) represents the amount of thermos-vaporized free-hydrocarbons during pyrolysis process under an inert N2 atmosphere. S2 peak (units of mg HC/g, the milligram hydrocarbon per gram of rock) is associated with the thermal cracking of heavier and long chain hydrocarbons for the remaining hydrocarbon potential. TOC content, representing OM richness, is also obtained for further analysis.

3.6. Low-pressure CO_2/N_2 gas adsorption (LP- CO_2/N_2 -GA)

LP-CO₂/N₂-GA experiments were carried out to obtain pore structure attributes (e.g., isotherm adsorption/desorption curves, PSD, SSA, PV). Prior to the experiments, shale fragments were crushed between 80 and 60 meshes and degassed at 80 °C over 8 h to guarantee the maximal cleanness of pore surface and preserve the pore structure of the samples (Yuan et al., 2018). Gas adsorption/desorption volume was measured with the relative equilibrium adsorption pressure (P/P_0) ranging from 0.01 to 0.99, where P is the gas vapor pressure in the system and P_0 is the saturation pressure of gas.

LP-CO₂-GA and LP-N₂-GA was conducted on Micromeritics® TriStar Plus apparatus under 273.1 K (eq. 0 °C), and Micromeritics® TriStar 3020 instrument under 77.4 K (eq. -195 °C), respectively. Properties of micropores (pore sizes range from 0.35 to 2 nm) and meso/macropores (pore sizes larger than 2 nm) were separately determined from LP-CO₂-GA and LP-N₂-GA (Yuan et al., 2021b). The micropores' PSD and PV were derived from CO₂ adsorption branch using nonlocal density functional theory (NLDFT) and Dubinin-Astakhov model (Dubinin and Astakhov, 1971; Neimark et al., 2009), respectively. The meso/macropores' PSD and SSA were derived from N₂ adsorption branch of isotherm using density functional theory (DFT) (Seaton and Walton, 1989; Lastoskie et al., 1993) and Brunauer-Emmett-Teller (BET) model (Barrett et al., 1951), respectively.

3.7. Slim compact micro imager (SCMI) and well loggings

SCMI data was collected by Weatherford from the well Theia-1 for structural interpretation. The Weatherford CMI 2.4 is a slim line compact micro imager tool that enables the measurement of conductivity. The SCMI tool is an eight arm, six calipers (two opposed diameters, four radii) and eight-pad microresistivity device generally applied in water-base muds, and demonstrates a high vertical resolution of 5 mm. The SCMI logging had been run at the interval from 1188.5 to 1593.2 m that covers Goldwyer I, Goldwyer II and Goldwyer III Formations (Molyneux et al., 2016).

Additionally, caliper logs, gamma-ray log (GR), density porosity & photo electric factor (PEF), sonic log, and resistivity logs were conducted along the entire interval from 1188.5 to 1593.2 m. Caliper logs were utilized for fundamental quality control and the assessment of borehole condition, and to identify the intervals that

may suffer from the potential severe washout, hole spiral and other features that could influence the results quality. Detailed results and discussion have been carried out in the following sections.

4. Results and discussion

To distinguish the favorable lithofacies of 'sweet-spot' interval. and further reveal the coupling relationships between 'sweet-spot' favorable lithofacies and petrophysical properties, we characterize Goldwyer I (Fig. 3, Fig. 4), Goldwyer II (Fig. 5, Fig. 6) and Goldwyer III (Figs. 7–9) using multi-scale technologies. The testing results include gamma-ray (GR) logging (Fig. 3a, Fig. 5a, and Fig. 7a), density porosity & PET logging (Fig. 3b, Fig. 5b, and Fig. 7b), sonic logging (Fig. 3c, Fig. 5c, and Fig. 7c), resistivity logging (Fig. 3d, Fig. 5d, and Fig. 7d), Slim-Compact Micro Imager (SCMI) resistivity (Figs. 3e and Fig. 5e, and Fig. 7e), TF image lithofacies (Fig. 3f, Fig. 5f, and Fig. 7f), TF image lithofacies associations (Fig. 3g, Fig. 5g, and Fig. 7g), mineralogical composition (Fig. 3h, Fig. 5h, and Fig. 7h), organic geochemical properties (Fig. 3i, Fig. 5i, and Fig. 7i), and petrophysical properties (e.g., pore shape, SSA, pore volume and PSD) obtained from laboratory experiments (Figs. 8 and 9), which will be described and discussed in the following sections.

4.1. Petrophysical well loggings

Petrophysical well logging data are compacted and shown for Goldwyer I, II and Goldwyer III. Three major lithologies are identified as (i) mudstones, (ii) limestones, and (iii) calcareous mudstones. The mudstone lithologies correspond to the intervals with high GR values (GR_{mean} > 150 API). Comparing between Goldwyer I, II and III, a large mudstone interval is observed in Goldwyer III, whereas a small mudstone proportion is shown in Goldwyer II (Figs. 3, 5 and 7). Density logs and neutron porosity logs, plotted at a scale of 1.95-2.95 g/cc and 0.45-0.15 v/v, respectively, demonstrate a variable shale crossover pattern. The density, neutron porosity, and PEF logging responses of mudstone lithology present the mean value in the range of 2.55-2.64 g/cc, 0.22-0.28 v/v, and 3–3.6 brne, respectively. Sonic log shows slow responses, with the mean values ranging from 88 to 95 μs/ft. Resistivity log responses are low with a mean in the range from 2 to 7 ohmm (Molyneux et al., 2016).

The limestone lithologies (e.g., the lower Goldwyer II member from the depth from 1399.5 to 1472.6 m) are characterized by low GR log responses (GR_{mean} from 46 to 71 API), while density and neutron porosity cross-over present to be weak and thin. The mean PEF values are higher (4.1–4.3 brne). Sonic log response is characterized by a relatively fast mean value (56–64 μ s/ft). The resistivity log shows a high mean value (17–42 ohmm).

The calcareous mudstone, referred to as the undifferentiated dolomitic and limy mudstone, is a mixed carbonate-siliciclastic lithology. The intervals are characterized by intermediate mean GR values (GR_{mean} from 128 to 155 API), and moderately thick "mudstone" density porosity cross-over when plotted on conventional scales. The sonic log and resistivity log both present intermediate mean responses, in the range of 75–83 $\mu s/ft$ and 4–18 ohmm, respectively.

4.2. SCMI resistivity images

Fig. 3e demonstrates the data obtained from the Weatherford CMI 2.4. With the assistance of SCMI resistivity images, the formation fractures are identified and categorized into conductive, resistive and mixed types. Goldwyer I is characterized by conductive fractures and mixed fractures (Fig. 3e), demonstrating a radial distribution and a weak NW-SE trend, respectively. Goldwyer II

develops a sparse distribution of fractures with a NW-SW strike trend (Fig. 5e). Unlike Goldwyer I and II, Goldwyer III is dominated by mixed fractures with a high angle to sub-vertical features (Fig. 7e) (Molyneux et al., 2016).

4.3. Lithology and lithofacies

Goldwyer I, II and III show a large variation in lithology and lithofacies (Table 1). Goldwyer I involves five principal lithologies, including (1) silty claystones (Fig. 4A1—A5) that are widely developed in the upper and middle section of the unit, (2) argillaceous limestones (Fig. 4B1—B3) that are characterized by calcitic matrix and fossil fragments, (3) dolomitic limestones (Fig. 4C1), (4) argillaceous siltstones (Fig. 4D1—D2), and (5) calcite-rich siltstones (Fig. 4E1). Goldwyer I widely develops the structure of silt-rich or clay-rich laminae and burrows (Fig. 4A1—A5). The principal framework grains are detrital quartz and detrital clays, with minor mica and pyrite serving as cements. Low TOC content is shown in the whole interval. The micropores are the principal pore type, which is widely developed between between minerals such as detrital clays and the micritic calcite crystals (Fig. 4A1—A5; Fig. 4B1—E1).

Goldwyer II member (1366.0–1472.6 m) is exclusively characterized by a higher proportion of limestone lithologies (Fig. 5). Mineralogical composition shows an abundance of calcite content, followed by quartz and dolomite, whereas the clays are fairly less than that in Goldwyer I. The calcareous mudstones (i.e., laminated calcareous mudstones, nodular calcareous mudstones) are mainly developed in the upper layer. Various lithologies are mixed in the middle layer, whereas the limestones (i.e., laminated limestones, nodular limestones) dominantly occupy the large proportion. Fig. 6 shows the lithologies of some representative samples in Goldwyer II, including (1) calcareous claystones (Fig. 6A1), (2) silty claystones (Fig. 6B1), and (3) argillaceous limestone (Fig. 6C1–C2). Overall, these sediments are interpreted to deposit in a mixed carbonate - siliciclastic setting, and periodically interrupted by increased siliciclastic input.

Regarding the TF image lithofacies, when comparing between Goldwyer I and II (Fig. 3f and Fig. 5), interestingly, the mottled limestone, nodular limestone and laminated limestone lithologies are commonly developed in Goldwyer II, whereas they are rarely shown in Goldwyer I. This indicates that Goldwyer II are highly influenced by the post-depositional diagenesis processes, which could highly possibly result in larger vuggy porosity that is associated with micro-organisms from mid ramp settings (Fig. 5 g).

Goldwyer III member (1472.6–1593.2 m) develops an enormous amount of mudstone lithofacies (Fig. 7). Mudstone lithologies totally constitute 53.4% of the image lithofacies in the whole Theia-1 interval, while a large amount proportion is shown in Goldwyer III. Unlike Goldwyer I and II, Goldwyer III is predominantly comprised of nodular mudstone textures (Fig. 7f). Apart from nodular mudstone lithologies, Goldwyer III also presents an abundant amount of laminated mudstone lithologies, which indicates a low-energy depositional environment. Lithofacies association presents a dominant outer ramp setting in the whole interval. What's worth mentioning, the calcareous mudstone lithologies, which are commonly found in Goldwyer I and II, are rarely developed in Goldwyer III member. In Section 4.5, representative mudstone samples were selected from Goldwyer III as the main target for the coupling of lithofacies and laboratory petrophysical analysis.

4.4. Mineralogical and geochemical properties

Mineralogical and geochemical results demonstrate a large

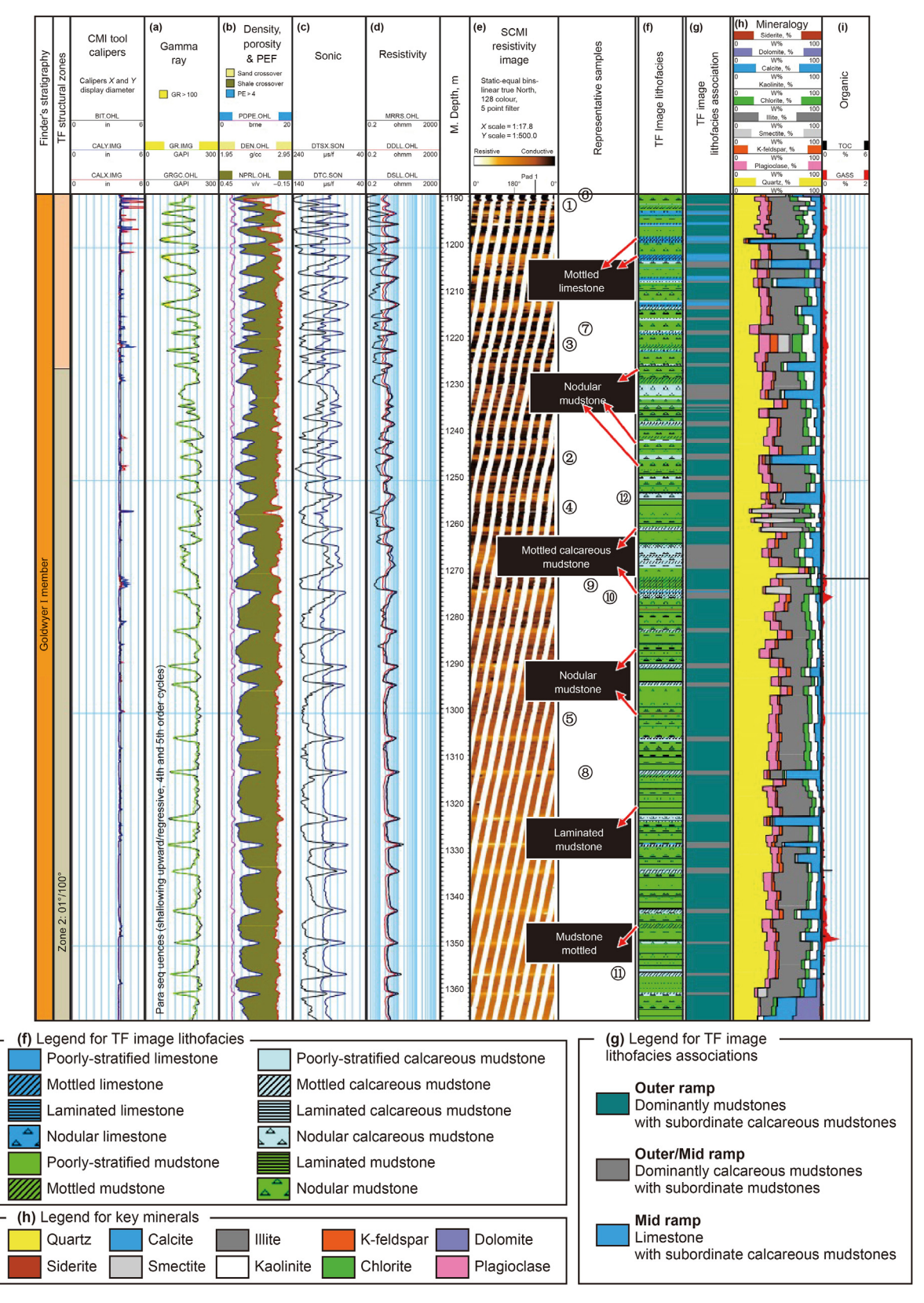


Fig. 3. Synthesis of well logging, lithological, mineralogical and geochemical properties of Goldwyer I interval (~1188.5—1366.0 m) via Theia-1 well. Well logging data include: (a) gamma-ray, (b) density porosity and PEF, (c) Sonic (d) resistivity, and (e) SCMI resistivity image data. Lithological data include (f) TF Image lithofacies, and (g) TF Image lithofacies ssociations. (h) Mineralogical composition and (i) geochemical data. Original data were adapted from Molyneux et al. (2016). Note that the numbers from ① to ② are representative samples correspond to the core pictures and samples shown in Fig. 4.

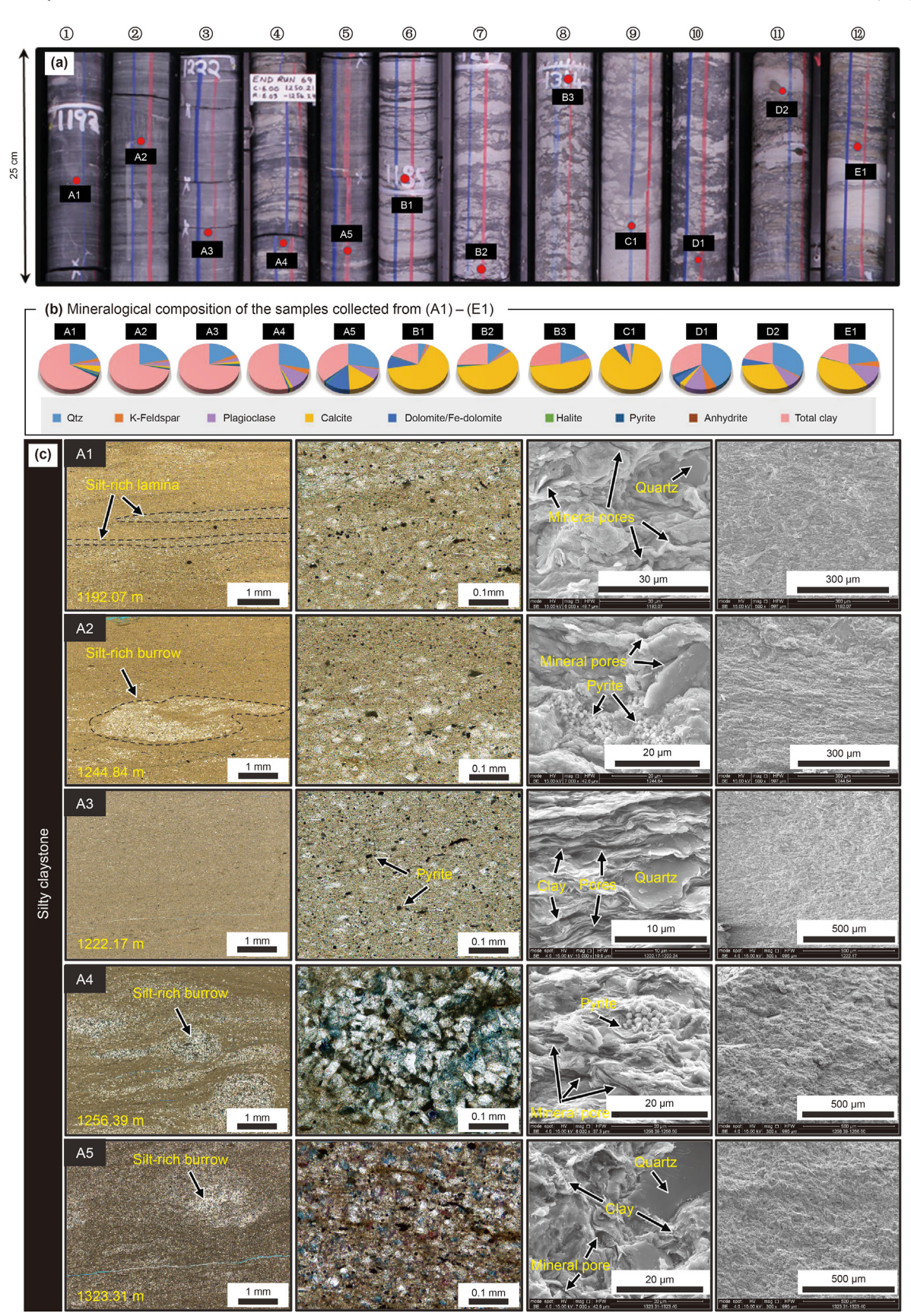


Fig. 4. Synthesis of petrological properties of the representative samples from Goldwyer I interval (~1188.5—1366.0 m) via Theia-1 well. The data include: (a) core images, (b) the pie chart displaying mineralogical composition, and (c) thin-section and SEM images of different lithologies, including [A1–A5] silty claystone, [B1–B3] argillaceous limestone, [C1] dolomitic limestone, [D1–D2] argillaceous siltstone, and [E1] calcite-rich siltstone. Some data were adapted from Department of Mines and Petroleum (2015).

variation between different Goldwyer members. Goldwyer I (1188.5–1366.0 m), Goldwyer II (1366.0–1472.6 m), and Goldwyer III (1472.6–1593.2 m) are characterized by high total clays, high

calcite/dolomite, and high illite content, respectively. Total clays are comprised of illite, chlorite, kaolinite, and smectite, from which illite is performed as the dominant clay type. Organic geochemical

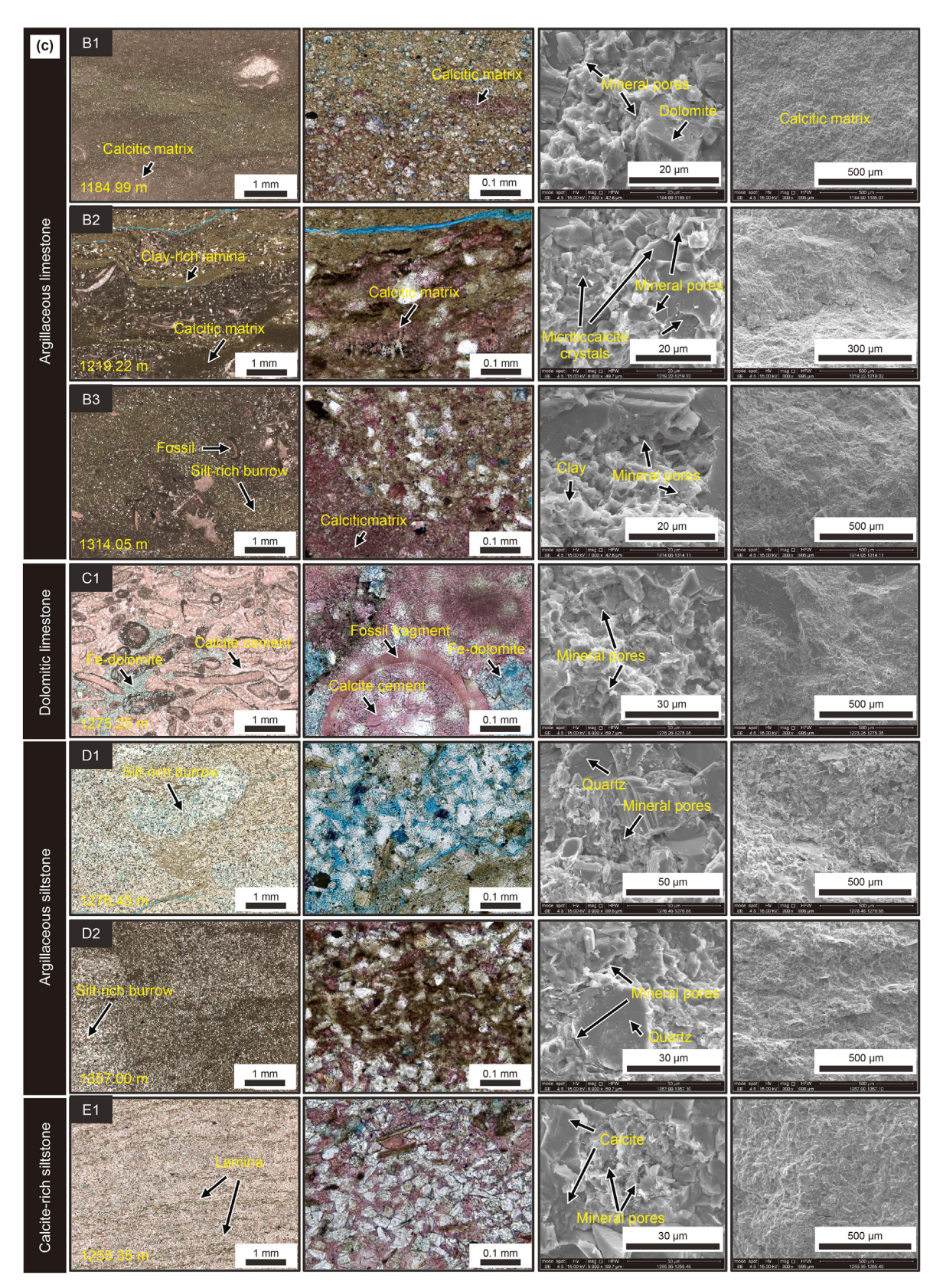


Fig. 4. (continued).

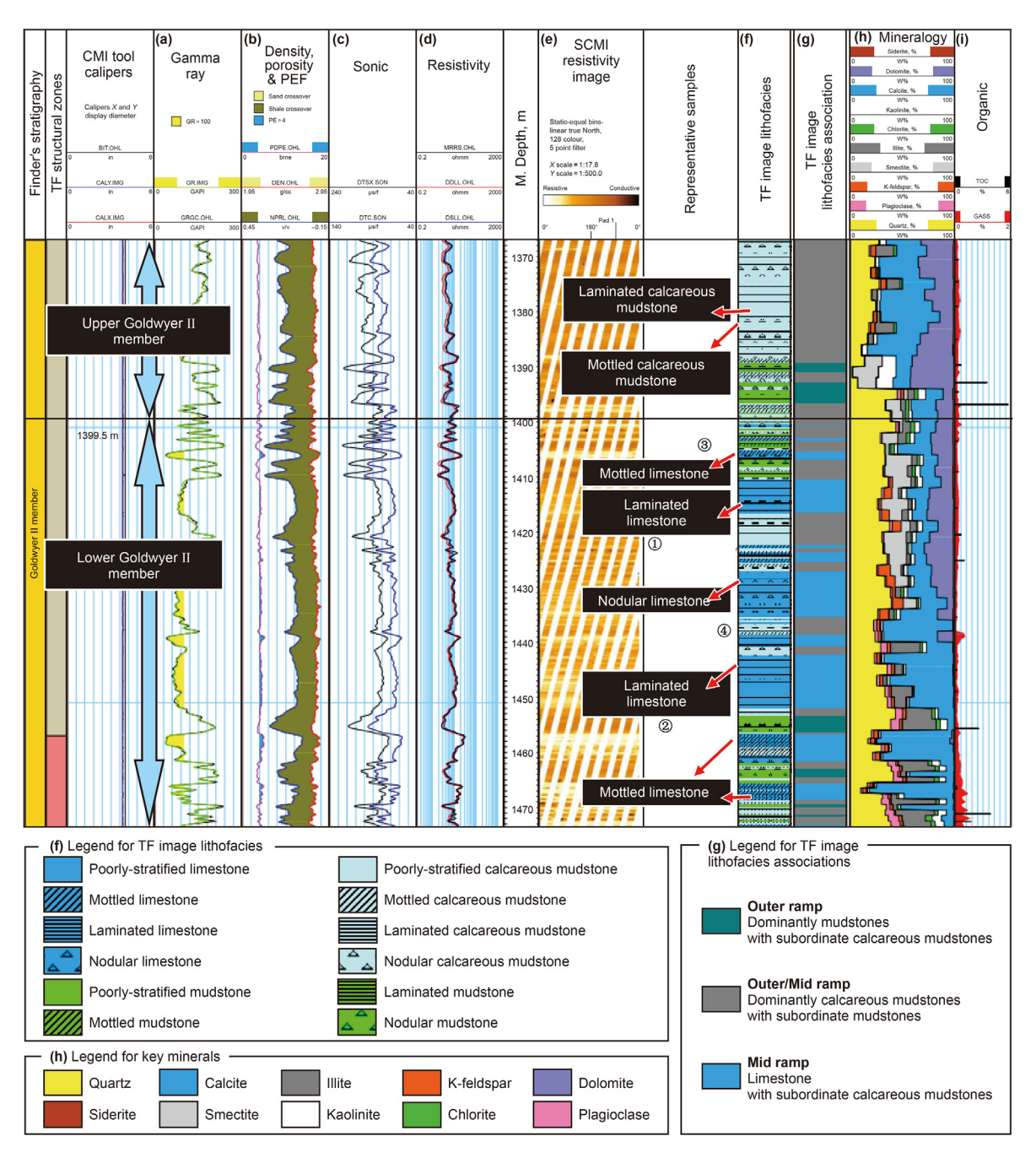


Fig. 5. Synthesis of well logging, lithological, mineralogical and geochemical properties of Goldwyer II interval (~1366.0—1472.6 m) via Theia-1 well. Well logging data include: (a) Gamma-ray, (b) Density porosity and PEF, (c) Sonic (d) Resistivity, and (e) SCMI resistivity image. Lithological data include (f) TF Image lithofacies, (g) TF Image lithofacies sssociations, (h) Mineralogical composition, and (i) Geochemical data. Data were adapted from Molyneux et al. (2016). Note that the numbers from ① to ④ are representative samples corresponding to the core pictures and samples shown in Fig. 6.

data highlighted the intervals containing the highest TOC and GASS content in Goldwyer III member at the depth of 1506–1525 m and 1551–1580 m, which are identified as the 'sweet-spot' intervals. Large amount of laminated mudstone lithologies are found in 'sweet-spot' intervals Fig. 7.

As per mineralogical and geochemical criteria, the representative mudstones from 'sweet-spot' intervals in Goldwyer III are subdivided into: the laminated argillaceous OM-rich, argillaceous OM-moderate/poor, calcareous OM-rich, calcareous OM-moderate/poor, mixed OM-rich, and mixed OM-moderate/poor types (Yuan et al., 2021a).

4.5. Petrophysical properties

To identify the most favorable lithologies and lithofacies of stratigraphic 'sweet-spot' interval in Goldwyer III, and unveil the coupling relationships between macroscopic 'sweet-spot' interval characteristics and their microscopic pore structure attributes (e.g., pore morphology, pore volume (PV), specific surface area (SSA), pore size distribution (PSD), and adsorption/desorption isotherm), the results obtained from Ar-SEM and low-pressure CO_2/N_2 gas adsorption were discussed in sections below.

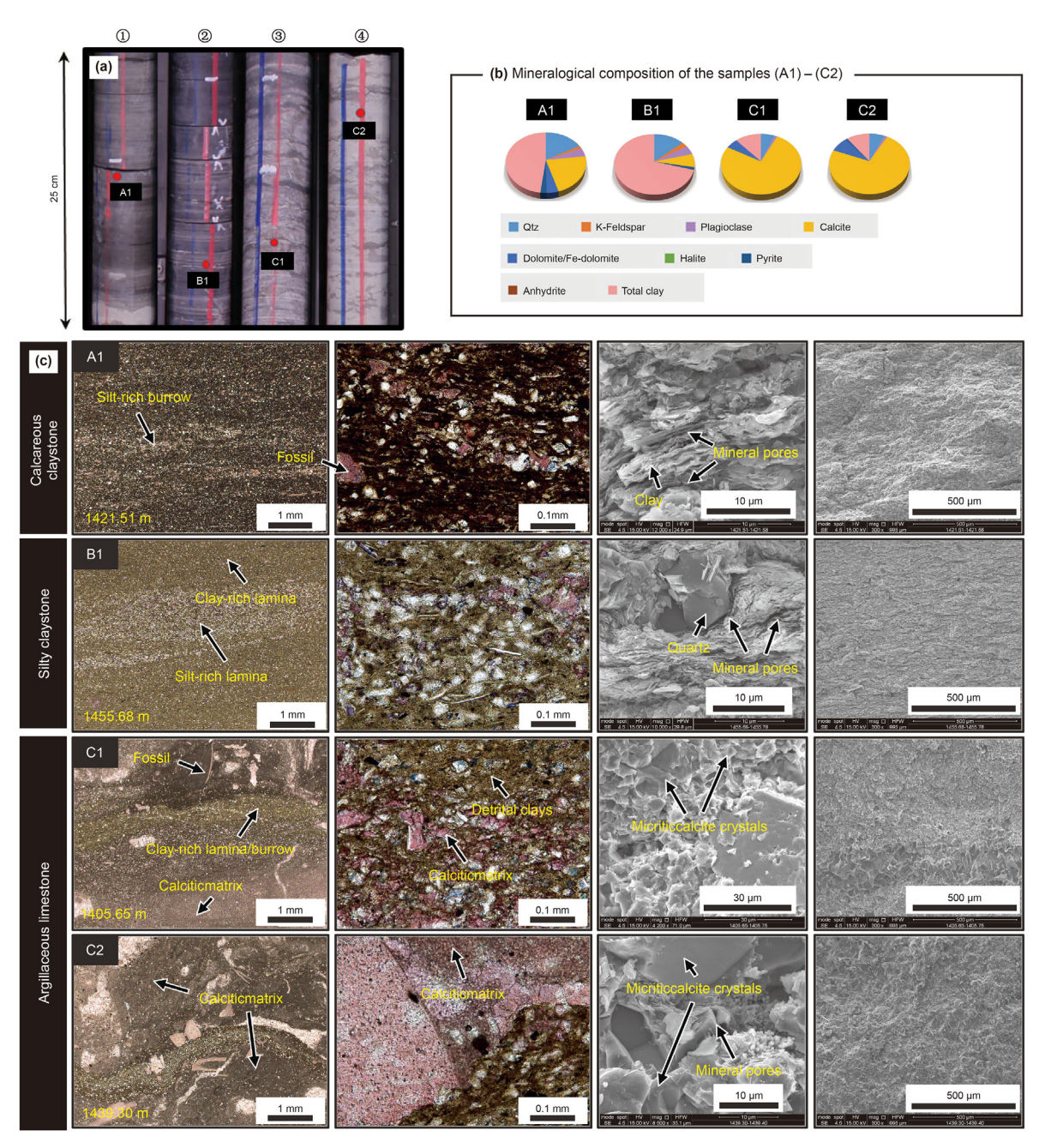


Fig. 6. Synthesis of petrological properties of the representative samples ([A1], [B1], [C1] and [C2]) in Goldwyer II interval (~1366.0—1472.6 m) via Theia-1 well. The data include: (a) Core images, (b) the pie chart displaying the mineralogical composition, and (c) thin-section and SEM images of the heterogeneous lithofacies. The lithofacies were classified into: [A1] Calcareous claystone, [B1] Silty claystone, and [C1–C2] Argillaceous Limestone. Some data were adapted from Department of Mines and Petroleum (2015).

4.5.1. Pore morphology and pore types from Ar-SEM

Ar-SEM results reveal that the representative mudstone samples from Goldwyer III develop both OM pores and mineral pores (e.g., intra-particle (Intra-P) and inter-particle (Inter-P) pores) (Fig. 8). OM pores, which are created owing to hydrocarbon expulsion after OM cracking (Jarvie et al., 2007; Loucks and Ruppel, 2007; Milliken et al., 2013), are intensively shown in forms of circular-/bubble-/spherical-shapes and are predominately attributed to the large SSA (Mastalerz et al., 2013). Some larger OM pores, showing in ellipsoid shape with the pore length stretching up to 2 μ m, present a well-connected manner and could contribute to a large PV intimated with free gas storage capacity (Loucks et al., 2012) (Fig. 8a1–f1).

These large pore lengths can be produced from the combination of micro-/mesopores as the thermal maturation reached higher (Chen and Xiao, 2014).

Mineral pores in Goldwyer III mudstone samples are observed in different shapes that was related to the pore evolution process. There are inter-particle (interP) and intercrystalline pores with larger pore diameters commonly developed between detrital minerals such as quartz or feldspar and matrix material (Fig. 8a2–f2). IntraP/intracrystalline pores are rarely found in argillaceous lithofacies but are commonly developed in calcareous accumulations (Fig. 8d2).

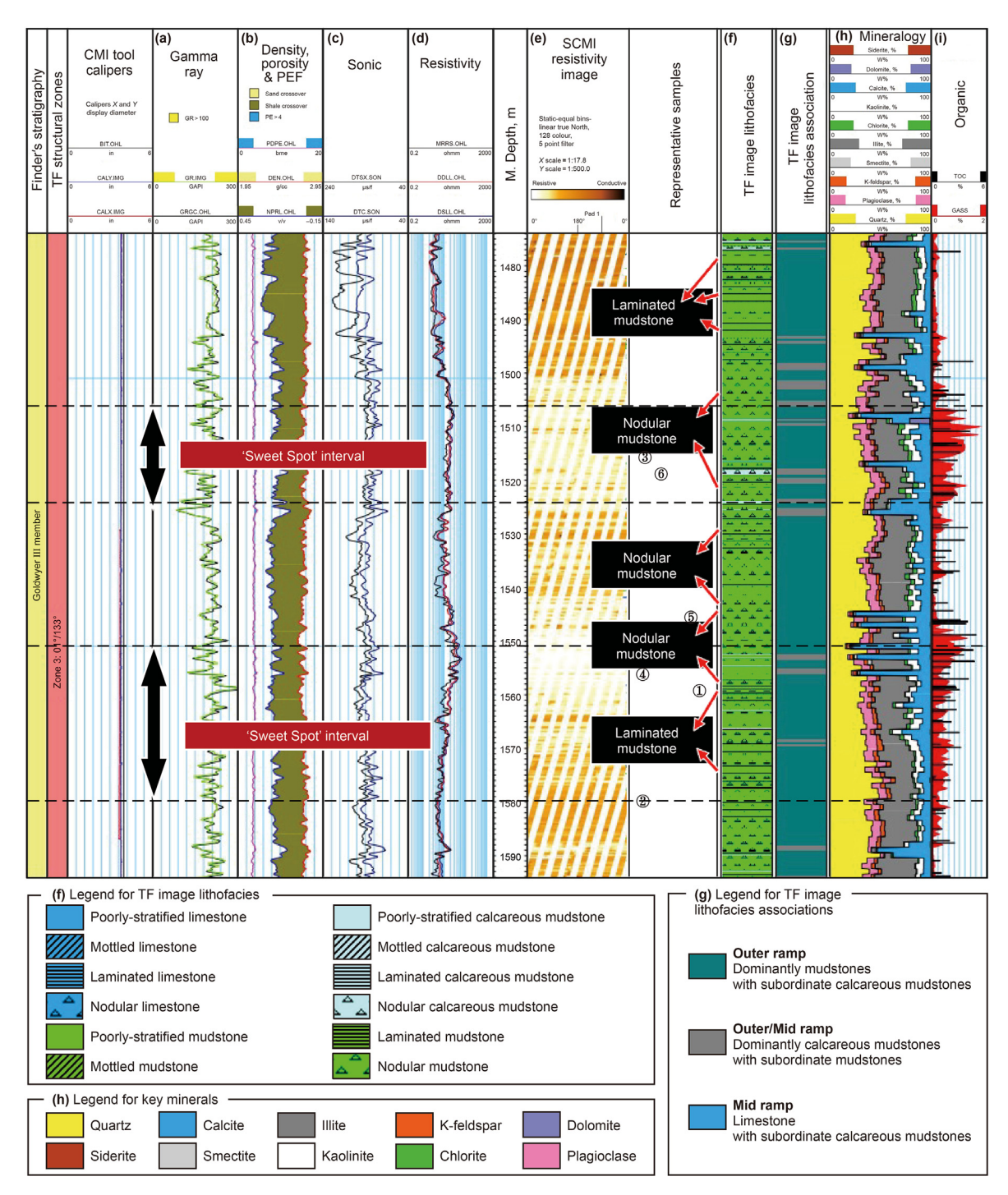


Fig. 7. Synthesis of well logging, lithological, mineralogical and geochemical properties of Goldwyer III interval (1472.6–1593.2 m) via Theia-1 well. Well logging data include: (a) Gamma-ray, (b) Density porosity and PEF, (c) Sonic (d) Resistivity, and (e) SCMI resistivity image. Lithological data include (f) TF Image lithofacies, (g) TF Image lithofacies associations, (h) Mineralogical composition, and (i) Geochemical data. Data were adapted from Molyneux et al. (2016). Note that the numbers from ① to ⑥ are representative samples corresponding to the core pictures and samples from [A] to [F] shown in Figs. 8 and 9.

4.5.2. Pore volume (PV), specific surface area (SSA) and pore size distribution (PSD) interpreted from LP-CO₂/ N_2 -GA

PV, SSA and PSD in the full pore range (pore size between 0.3 and 200 nm) were calculated and plotted in a bar chart, with the accumulative distributions depicted in the same figure (Fig. 9A1–F1, A2–F2, A3–F3). Fig. 9 shows a total of six lithofacies, with each lithofacies represented by one typical sample (i.e., G#1, G#2, G#3, G#4, G#5, G#6 represent the laminated argillaceous

OM-rich, argillaceous OM-poor, calcareous OM-rich, calcareous OM-poor, mixed OM-rich, and mixed OM-poor mudstone, respectively).

The laminated argillaceous mudstone (G#1 and G#2) shows an extraordinarily high value distribution in $PV_{2-17\ nm}$ and $PSD_{2-17\ nm}$, whereas other lithofacies demonstrate less (see the highlighted blue area in Fig. 9A1–F1, and A3–F3). For example, the accumulative $PV_{2-17\ nm}$ of the laminated argillaceous mudstone G#1 and

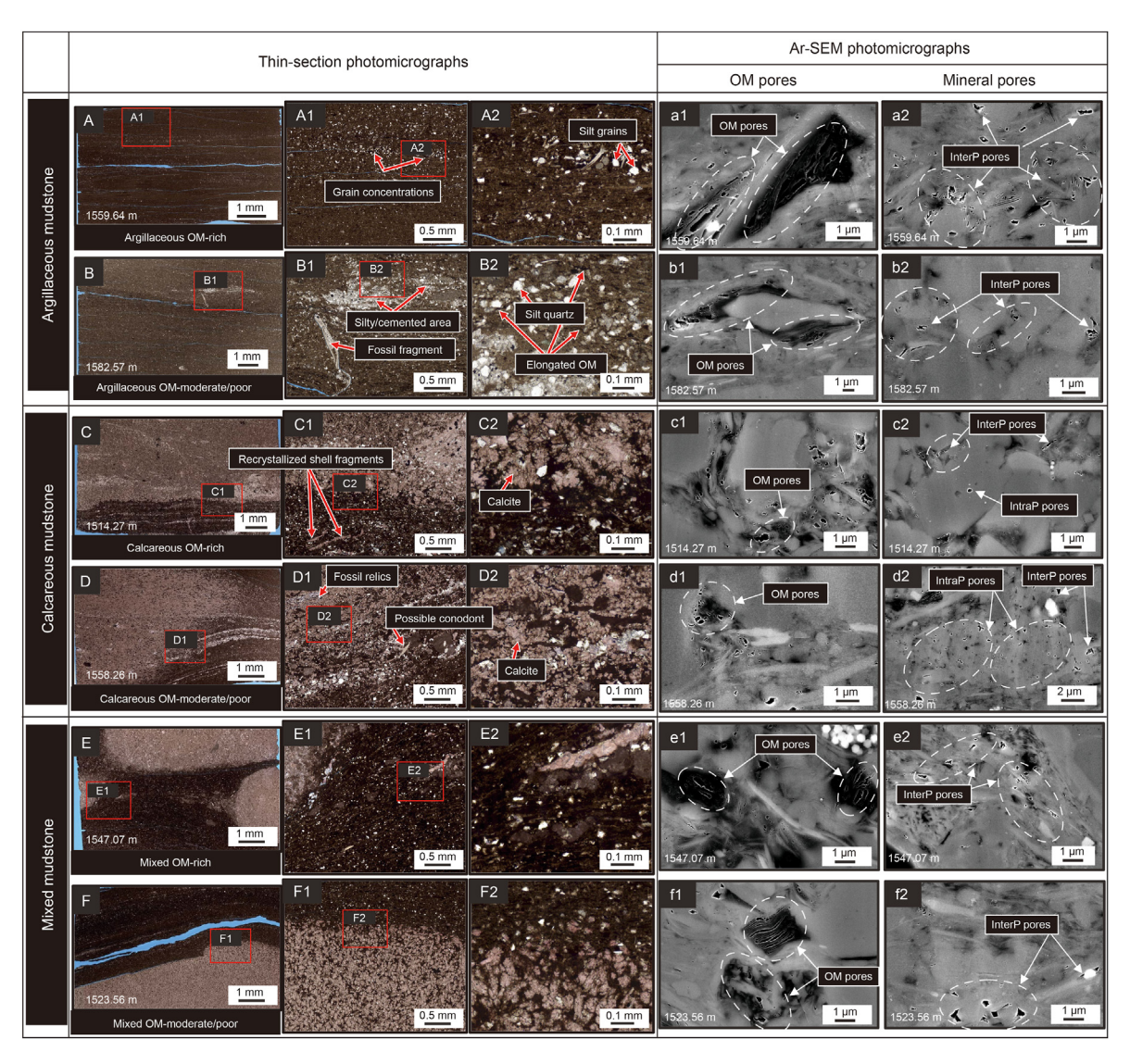


Fig. 8. Thin-sention and Ar-SEM images of the representative mudstone samples (from [A] to [F]) in Goldwyer III interval (1472.6–1593.2 m) via Theia-1 well. The lithofacies were classified into: [A] argillaceous OM-rich mudstone, [B] argillaceous OM-moderate/poor mudstone, [C] calcareous OM-rich mudstone, [D] calcareous OM-moderate/poor mudstone, [E] mixed OM-rich mudstone, [F] mixed OM-moderate/poor mudstone. The Ar-SEM results of [a1]–[f1] show OM pores, whereas [a2]–[f2] show inorganic pores. The Ar-SEM images were obtained from Weatherford Co. Some data were adapted from Yuan et al. (2021a) and Department of Mines and Petroleum (2016).

G#2 is 1.65 and 1.44 cm³/100 g, respectively; whereas the calcareous mudstone G#3 and G#4 are 1.18 and 0.99 cm³/100 g, and the mixed mudstone G#5 and G#6 are 0.80 and 0.88 cm³/100 g, respectively. This can be attributed to the pore sizes ranging from 2 to 17 nm, which are prominantly contributed by clays in the studied samples (Yuan et al., 2021a).

Apart from $PV_{2-17\ nm}$ and $PSD_{2-17\ nm}$, the laminated argillaceous OM-rich mudstone (G#1), in particular, also shows an extraordinarily high value distribution in $SSA_{<2\ nm}$, which is owing to the synthetic effect from high clay and TOC content (Yuan et al., 2021a). As shown in highlighted blue area of Fig. 9A2–F2, for example, the accumulative $SSA_{<2\ nm}$ of argillaceous OM-rich mudstone G#1 is 3.24 m²/g, whereas argillaceous OM-poor G#2 is 2.48 m²/g. By contrast, the calcareous mudstone G#3 and G#4 are 1.76 and 1.75 m²/g, and the mixed mudstone G#5 and G#6 are 3.23 and 2.50 m²/g, respectively. Considering that $PV_{2-17\ nm}$ is critical parameters contributed by clay mineral pores for free gas, whereas $SSA_{<2\ nm}$ is attributed to OM pores for adsorbed gas (Yuan et al., 2019c), it is thus concluded that the laminated argillaceous OM-rich mudstone is the

most favorable and excellent lithofacies for gas storage capacity this is associated with 'sweet-spot' intervals in Goldwyer formation.

$4.5.3. \; Gas \; adsorption \; isotherm$

Shale adsorption properties are highly corelated with lithologies and lithofacies (Ross and Bustin, 2009). Fig. 9A4–F4 shows the adsorption isotherms determined from LP-N2-GA. The laminated argillaceous OM-rich mudstone (G#1) shows the largestest N2 adsorption amount. For example, the maximum adsorption amount of G#1 is 26.1 cm³/g STP, whereas other lithofacies show less than 20 cm³/g STP (e.g., the argillaceous OM-poor G#2 shows 23.2 cm³/g STP, whereas the the calcareous mudstone G#3 and G#4 are 18.0 and 13.8 cm³/g STP, and the mixed mudstone G#5 and G#6 are 13.2 and 12.8 cm³/g STP, respectively). G#1 also presents the largest hysteresis gap between the adsorption and desorption curves.

5. Conclusions

The identification of stratigraphic 'sweet-spot' interval is crucial

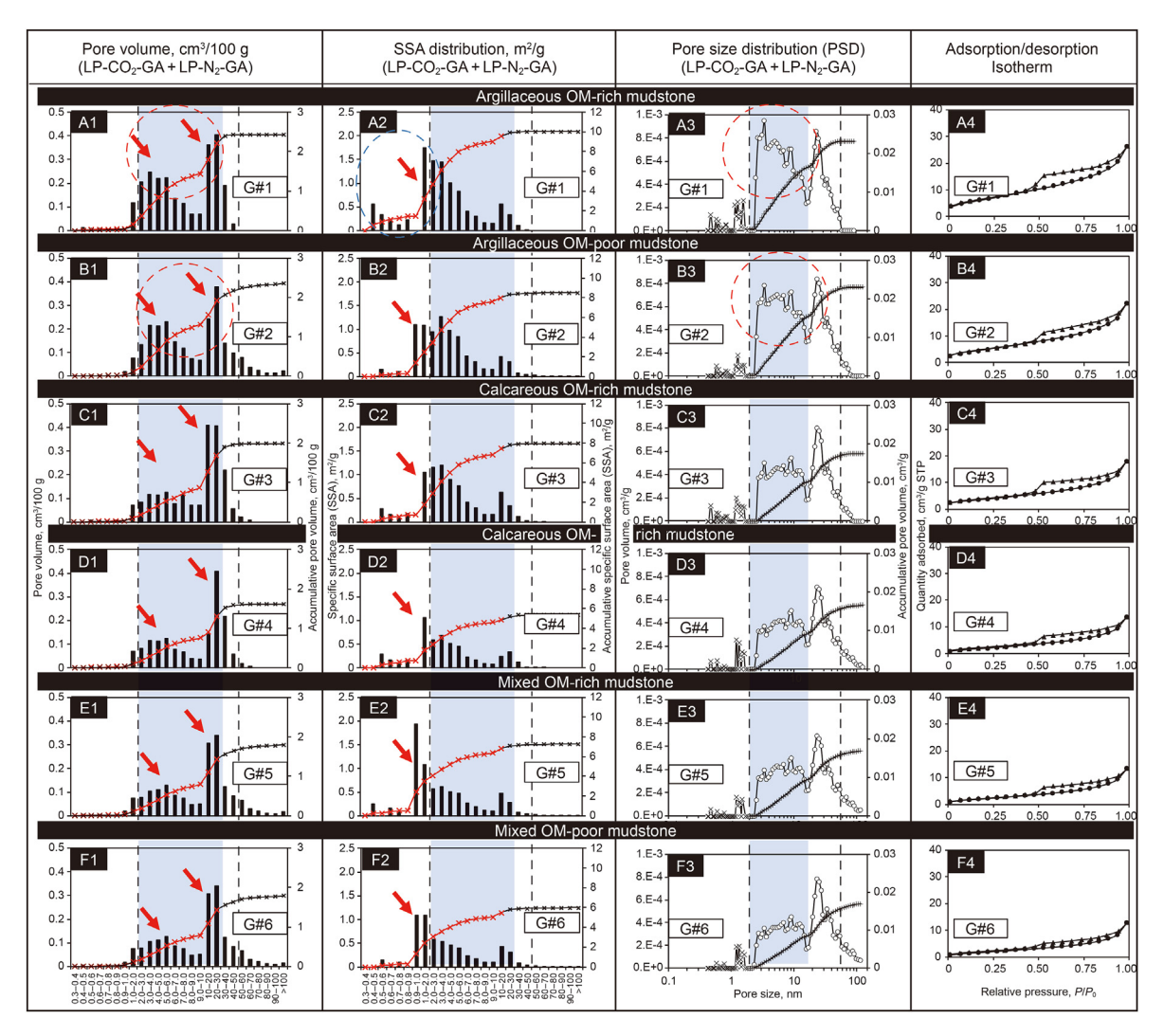


Fig. 9. Petrophysical properties (obtained from LP-CO₂/N₂-GA) of the representative mudstone samples in Goldwyer III interval (1472.6–1593.2 m) via Theia-1 well. Note that the sample ID is G#1-G#6 that corresponds to the sample of [A]-[F] in Fig. 8. The results of [A1]-[F1] demonstrate pore volume (PV, cm³/100 g), [A2]-[F2] exhibit specific surface area (SSA, m²/g), [A3]-[F3] show pore size distribution (PSD), and [A4]-[F4] show adsorption/desorption isotherm.

for accurate resource estimation. Despite that the large advanced approaches have developed and gained progress on formation evaluation, they are highly restricted on application in heterogeneous lithofacies due to the limited resolution, thus resulting in large uncertainties. In this study, we used quantitative and qualitative analysis in a high-resolution, from in-situ macroscopic scale to laboratory microscopic scale, for the purpose to identify the stratigraphic 'sweet-spot' interval with high accuracies.

A multiscale study, using advanced well logging, SCMI technologies and the laboratory petrophysical and compositional experiments, enables the identification of the stratigraphic 'sweetspot' interval in Goldwyer Formation. The 'sweet-spot' interval, developing the most favorable and productive lithofacies, is located in Goldwyer III at the depth from 1551 to 1580 m and from 1506 to 1525 m. Those 'sweet-spot' intervals are featured by a high proportion of the laminated argillaceous OM-rich mudstone (average clays > 50%; TOC > 2%), containing large amount of OM pores and interP pores with high-quality petrophysical properties in SSA, PV, PSD and gas adsorption capacity.

Goldwyer I (1188.5–1366.0 m), which is comprised of thick mudstone interval (75.1%) interbedded with thin calcareous

mudstone (21.3%) and minor limestone (2.7%) lithofacies, was deposited in an environment of outer ramp setting. Goldwyer II (1366.0–1472.6 m), containing less mudstone (15.4%) but a high proportion of calcareous mudstone (49.7%) and fair limestone (35%), can be split into two members: (i) the upper section (1366–1399.5 m) involves calcareous mudstone (83.9%), mudstone (16.1%) and no limestone, deposited in a transitional middle to outer ramp setting; whereas (ii) the lower section (1399.5–1472.6 m), comprising limestone (50.9%), calcareous mudstone (34.1%) and thin mudstone lithofacies (15%), deposited in a middle ramp and transitional middle to outer ramp.

The whole Goldwyer III member (1472.6—1593.2 m) covers a large thickness of mudstone interval (94.4%) interbedded with a very thin calcareous mudstone (5.5%). The most favorable lith-ofacies of stratigraphic 'sweet-spot' interval develop numerous nanopores including OM pores and interP pores. A large proportion of mesopores ranging from 2 to 17 nm, is developed and greatly contributed to PV that is intimated with free gas capacity. Meanwhile, micropores are also well-connected and widely distributed within thermal-matured OM and contributes to SSA that is associated with adsorbed gas capacity.

Table 1
A comparison of lithological, mineralogical and geochemical properties of Goldwyer I (1188.5—1366.0 m), Goldwyer II (1366.0—1472.6 m) and Goldwyer III (1472.6—1593.2 m) intervals via Theia-1 well of Goldwyer Formation, Canning Basin, WA. Original data were adapted from Molyneux et al. (2016).

Formation	Depth, m	TOC	Lithofacies		Facies Associations	
Goldwyer I	1188.5-1366.0	Low	Mudstone: 75.1 % Calcareous Mudstone: 21.3 % Limestone: 2.7 %		22% 3% 75%	
Goldwyer II	Upper 1366.0-1399.5	Low		Mudstone: 83.9 % Calcareous M: 16.0 % Limestone: 0 %		16%
	Lower 1399.5- 1472.6		Mudstone: 15.4 % Calcareous M: 49.7 % Limestone: 35 %	Mudstone: 50.9 % Calcareous M: 34.1 % Limestone: 15 %	53%	7% 54% 39%
Goldwyer III 1472.6-1593.2 High			Mudstone: 94.4 % Calcareous Mudstone: 5.5 % Limestone: 0 %		13%	
Legend for TF Image Lithofacies					Legend for TF Associations	Image Lithofacies
Poorly-stratified limestone			Poorl	y-stratified calcareous mudstone		
Mot	Mottled limestone			ed calcareous mudstone	Outer ramp	
Laminated limestone			Laminated calcareous mudstone		Outer/ Mid ramp	
Nodular limestone Poorly-stratified mudstone				Nodular calcareous mudstone Laminated mudstone Mid		
_				Nodular mudstone		
Mottled mudstone Nodular mudstone						

Acknowledgment

The authors appreciate the funding of the Fundamental Research Programme of Yunnan Province (202201AU070041), the funding of Yunnan University Young Talent Programme (CZ21623201), the funding of State Key Laboratory of Coal Mine Disaster Dynamics and Control in Chongging University (2011DA105287—FW202106), and the funding from the Key Laboratory of Deep-Earth Dynamics of Ministry of Natural Resources, under the Institute of Geology in Chinese Academy of Geological Sciences, Beijing (J1901). Much gratitudes for the Department of Mines, Industry Regulation and Safety under the Government of Western Australia for granting us the core samples under Approval Nos. G32825 & N00413. Thankfulness is also expressed to the Unconventional Gas Research Group at the discipline of Petroleum Engineering under Western Australian School of Mines, and the Microscopy & Microanalysis Facility of John De Laeter Centre in Curtin University, for their facility assistances.

References

Barrett, E.P., Joyner, L.G., Halenda, P.P., 1951. The determination of pore volume and area distributions in porous substances. I. Computations from nitrogen isotherms. J. Am. Chem. Soc. 73, 373—380. https://doi.org/10.1021/ja01145a126.

Brown, S., Boserio, I., Jackson, K., et al., 1984. The geological evolution of the Canning Basin-implications for petroleum exploration. Petroleum Exploration Society of Australia.

Cai, J.C., Wood, D.A., Hajibeygi, H., et al., 2022. Multiscale and multiphysics influences on fluids in unconventional reservoirs: modeling and simulation. Adv. Geo-Energy Res. 6, 91–94. https://doi.org/10.46690/ager.2022.02.01.

Chen, J., Xiao, X., 2014. Evolution of nanoporosity in organic-rich shales during thermal maturation. Fuel 129, 173–181. https://doi.org/10.1016/j.fuel.2014.03.058.

Coates, G.R., Xiao, L., Prammer, M.G., 1999. NMR Logging: Principles and Applications. Gulf Professional Publishing.

Curtis, M.E., Cardott, B.J., Sondergeld, C.H., et al., 2012. Development of organic porosity in the Woodford Shale with increasing thermal maturity. Int. J. Coal

Geol. 103, 26-31. https://doi.org/10.1016/j.coal.2012.08.004.

Department of Mines and Petroleum, 2014. Western Australia's Petroleum and Geothermal Explorer's Guide. Government of Western Australia.

Department of Mines and Petroleum, 2015. Detailed Petrological Evaluation of Core Samples of Theia-1 Well, Australia, Core Laboratories. Petroleum Services Job File No. 150953G.

Department of Mines and Petroleum, 2016. Shale Analysis of Theia 1 for Finder Exploration, Weatherford Laboratories (Australia) Pty. Ltd. File No.: AB-77969. Dubinin, M., Astakhov, V., 1971. Description of Adsorption Equilibria of Vapors on Zeolites over Wide Ranges of Temperature and Pressure. ACS Publications.

Eberzin, A., 1940. Middle and Upper Pliocene of the Black Sea Region: Statigrafiya SSSR: Neogene SSSR (Stratigraphy of the USSR: Neogene of the USSR), 8. Doklady Akademii Nauk SSSR, Moscow, pp. 477–566.

Forman, D., Wales, D., 1981. Geological Evolution of the Canning Basin, Western Australia. Bureau of Mineral Resources. Geology and Geophysics.

Gao, Z., Fan, Y., Xuan, Q., et al., 2020. A review of shale pore structure evolution characteristics with increasing thermal maturities. Adv. Geo-Energy Res. 4, 247–259. https://doi.org/10.46690/ager.2020.03.03.

Ge, X., Fan, Y., Deng, S., et al., 2016. An improvement of the fractal theory and its application in pore structure evaluation and permeability estimation. J. Geophys. Res. Solid Earth 121, 6333–6345. https://doi.org/10.1002/ 2016IB013074.

Geoscience Australia, 2007. Canning Basin Geological Summary.

Guan, M., Wu, S., Hou, L., et al., 2021. Paleoenvironment and chemostratigraphy heterogenity of the Cretaceous organic-rich shales. Adv. Geo-Energy Res. 5, 444–455. https://doi.org/10.46690/ager.2021.04.09.

Hu, Q., Ewing, R.P., Rowe, H.D., 2015. Low nanopore connectivity limits gas production in Barnett formation. J. Geophys. Res. Solid Earth 120, 8073–8087. https://doi.org/10.1002/2015/B012103.

Jarvie, D.M., Hill, R.J., Ruble, T.E., et al., 2007. Unconventional shale-gas systems: the Mississippian Barnett Shale of north-central Texas as one model for thermogenic shale-gas assessment. AAPG Bull. 91, 475–499. https://doi.org/10.1306/ 1219060668

Jiang, Z., Tang, X., Li, Z., et al., 2016. The whole-aperture pore structure characteristics and its effect on gas content of the Longmaxi Formation shale in the southeastern Sichuan Basin. Earth Sci. Front. 23, 126–134. https://doi.org/ 10.13745/j.esf.2016.02.013.

Kennard, J., Jackson, M., Romine, K., et al., 1994. Depositional Sequences and Associated Petroleum Systems of the Canning Basin. WA.

Krumbein, W.C., 1948. Lithofacies maps and regional sedimentary-stratigraphic analysis. AAPG Bull. 32, 1909–1923.

Kuuskraa, V., Stevens, S.H., Moodhe, K.D., 2013. Technically Recoverable Shale Oil and Shale Gas Resources: an Assessment of 137 Shale Formations in 41

Countries outside the United States, US Energy Information Administration. US Department of Energy.

- Lafargue, E., Marquis, F., Pillot, D., 1998. Rock-Eval 6 applications in hydrocarbon exploration, production, and soil contamination studies. Rev. Inst. Fr. Petrol 53, 421–437. https://doi.org/10.2516/ogst:1998036.
- Lastoskie, C., Gubbins, K.E., Quirke, N., 1993. Pore size distribution analysis of microporous carbons: a density functional theory approach. J. Phys. Chem. 97, 4786–4796. https://doi.org/10.1021/j100120a035.
- Lazar, O.R., Bohacs, K.M., Macquaker, J.H., et al., 2015. Capturing key attributes of fine-grained sedimentary rocks in outcrops, cores, and thin sections: nomenclature and description guidelines. J. Sediment. Res. 85, 230–246. https:// doi.org/10.2110/jsr.2015.11.
- Liu, B., Wang, H., Fu, X., et al., 2019a. Lithofacies and depositional setting of a highly prospective lacustrine shale oil succession from the Upper Cretaceous Qingshankou Formation in the Gulong sag, northern Songliao Basin, northeast China. AAPG Bull. 103, 405–432. https://doi.org/10.1306/08031817416.
- Liu, K., Ostadhassan, M., Hackley, P., et al., 2019b. Experimental study on the impact of thermal maturity on shale microstructures using hydrous pyrolysis. Energy Fuel. 33, 9702–9719. https://doi.org/10.1021/acs.energyfuels.9b02389
- Fuel. 33, 9702–9719. https://doi.org/10.1021/acs.energyfuels.9b02389. Loucks, R.G., Reed, R.M., Ruppel, S.C., et al., 2010. Preliminary Classification of Matrix Pores in Mudrocks.
- Loucks, R.G., Reed, R.M., Ruppel, S.C., et al., 2012. Spectrum of pore types and networks in mudrocks and a descriptive classification for matrix-related mudrock pores. AAPG Bull. 96, 1071–1098. https://doi.org/10.1306/08171111061.
- Loucks, R.G., Ruppel, S.C., 2007. Mississippian barnett shale: lithofacies and depositional setting of a deep-water shale-gas succession in the fort worth basin, Texas. AAPG Bull. 91, 579–601. https://doi.org/10.1306/11020606059.
- Luffel, D., Guidry, F., Curtis, J., 1992. Evaluation of Devonian shale with new core and log analysis methods. J. Petrol. Technol. 44, 1192–1197. https://doi.org/10.2118/ 21297-PA
- Mastalerz, M., Schimmelmann, A., Drobniak, A., et al., 2013. Porosity of Devonian and Mississippian New Albany Shale across a maturation gradient: insights from organic petrology, gas adsorption, and mercury intrusion. AAPG Bull. 97, 1621–1643. https://doi.org/10.1306/04011312194.
- Milliken, K.L., Rudnicki, M., Awwiller, D.N., et al., 2013. Organic matter—hosted pore system, Marcellus formation (Devonian), Pennsylvania. AAPG Bull. 97, 177—200. https://doi.org/10.1306/07231212048.
- Molyneux, I., Rideout, C., Mossadegh, Z., et al., 2016. Structural and Sedimentological Interpretation of SCMI Borehole Image Data. Finder Exploration Pty Ltd.
- Neimark, A.V., Lin, Y., Ravikovitch, P.I., et al., 2009. Quenched solid density functional theory and pore size analysis of micro-mesoporous carbons. Carbon 47, 1617–1628. https://doi.org/10.1016/j.carbon.2009.01.050.
- Passey, Q.R., Bohacs, K., Esch, W.L., et al., 2010. From oil-prone source rock to gasproducing shale reservoir-geologic and petrophysical characterization of unconventional shale gas reservoirs. Int. Oil Gas Conf. Exhib. China. https://doi. org/10.2118/131350-MS.
- Poppe, L.J., Paskevich, V.F., Hathaway, J.C., et al., 2001. A laboratory manual for X-ray powder diffraction. US Geol. Surv. Open File Rep. 1, 1–88.
- Rezaee, R., 2015. Fundamentals of Gas Shale Reservoirs. John Wiley & Sons. https://doi.org/10.1002/9781119039228.
- Ross, D.J., Bustin, R.M., 2009. The importance of shale composition and pore structure upon gas storage potential of shale gas reservoirs. Mar. Petrol. Geol. 26, 916–927. https://doi.org/10.1016/j.marpetgeo.2008.06.004.
- Rouquerol, J., Avnir, D., Fairbridge, C., et al., 1994. Recommendations for the characterization of porous solids (Technical Report). Pure Appl. Chem. 66, 1739–1758. https://doi.org/10.1351/pac199466081739.
- Seaton, N., Walton, J., 1989. A new analysis method for the determination of the pore size distribution of porous carbons from nitrogen adsorption measurements. Carbon 27, 853–861. https://doi.org/10.1016/0008-6223(89)90035-3.
- Slatt, R.M., Abousleiman, Y., Philp, P., et al., 2014. Sequence Stratigraphy, Geomechanics, Microseismicity, and Geochemistry Relationships in Unconventional Resource Shales, 25–27. Unconventional Resources Technology Conference, Denver, Colorado, pp. 327–342. https://doi.org/10.15530/urtec-

- 2014-1934195. August 2014.
- Slatt, R.M., Rodriguez, N.D., 2012. Comparative sequence stratigraphy and organic geochemistry of gas shales: commonality or coincidence? J. Nat. Gas Sci. Eng. 8, 68–84. https://doi.org/10.1016/j.jngse.2012.01.008.
- Sloss, L.L., 1950. Paleozoic sedimentation in Montana area. AAPG Bull. 34, 423-451.
- Sun, M., Zhang, L., Hu, Q., et al., 2019. Multiscale connectivity characterization of marine shales in southern China by fluid intrusion, small-angle neutron scattering (SANS), and FIB-SEM. Mar. Petrol. Geol., 104101 https://doi.org/10.1016/ imarnetgeo.2019.104101
- Van Hattum, J., Bond, A., Jablonski, D., et al., 2019. Exploration of an unconventional petroleum resource through extensive core analysis and basin geology interpretation utilising play element methodology: the Lower Goldwyer Formation, onshore Canning Basin, Western Australia. APPEA J. 59, 464–481. https:// doi.org/10.1071/A/18225.
- Walker, K.R., 1962. Lithofacies map of Lower Mississippian clastics of eastern and east-central United States. AAPG Bull. 46, 105—111.
- Wang, G., Carr, T.R., 2012. Methodology of organic-rich shale lithofacies identification and prediction: a case study from Marcellus Shale in the Appalachian basin. Comput. Geosci. 49, 151–163. https://doi.org/10.1016/j.cageo.2012.07.011.
- Wu, S., Yang, Z., Zhai, X., et al., 2019. An experimental study of organic matter, minerals and porosity evolution in shales within high-temperature and highpressure constraints. Mar. Petrol. Geol. 102, 377–390. https://doi.org/10.1016/ i.marpetgeo.2018.12.014.
- Xiao, L., Liao, G., Deng, F., et al., 2015. Development of an NMR system for downhole porous rocks. Microporous Mesoporous Mater. 205, 16–20. https://doi.org/10.1016/j.micromeso.2014.09.024.
- Xu, J., Wu, S., Liu, J., et al., 2021. New insights into controlling factors of pore evolution in organic-rich shale. Energy Fuel. 35, 4858–4873. https://doi.org/10.1021/acs.energyfuels.0c04189.
- Yang, R., He, S., Yi, J., et al., 2016. Nano-scale pore structure and fractal dimension of organic-rich Wufeng-Longmaxi shale from Jiaoshiba area, Sichuan Basin: investigations using FE-SEM, gas adsorption and helium pycnometry. Mar. Petrol. Geol. 70, 27–45. https://doi.org/10.1016/j.marpetgeo.2015.11.019.
- Yuan, Y., 2020. Multi-Scale Porosity and Pore Structure Assessment of Shale. Curtin University. http://hdl.handle.net/20.500.11937/81289.
- Yuan, Y., Rezaee, R., 2019a. Comparative porosity and pore structure assessment in shales: measurement techniques, influencing factors and implications for reservoir characterization. Energies 12, 2094. https://doi.org/10.3390/ en12112094.
- Yuan, Y., Rezaee, R., 2019b. Fractal analysis of the pore structure for clay bound water and potential gas storage in shales based on NMR and N2 gas adsorption. J. Petrol. Sci. Eng. 177, 756–765. https://doi.org/10.1016/j.petrol.2019.02.082.
- Yuan, Y., Rezaee, R., Al-Khdheeawi, E., et al., 2019c. Impact of composition on pore structure properties in shale: implications for micro/mesopore volume and surface area prediction. Energy Fuel. 33, 9619–9628. https://doi.org/10.1021/ acs.energyfuels.9b02232.
- Yuan, Y., Rezaee, R., Verrall, M., 2018. Pore characterization and clay bound water assessment in shale with a combination of NMR and low-pressure nitrogen gas adsorption. Int. J. Coal Geol. 194, 11–21. https://doi.org/10.1016/ i.coal.2018.05.003.
- Yuan, Y., Rezaee, R., Yu, H., et al., 2021a. Compositional controls on nanopore structure in different shale lithofacies: a comparison with pure clays and isolated kerogens. Fuel 303, 121079. https://doi.org/10.1016/j.fuel.2021.121079.
- Yuan, Y., Rezaee, R., Zou, J., et al., 2021b. Pore-scale study of the wetting behavior in shale, isolated kerogen, and pure clay. Energy Fuel. 35, 18459—18466. https:// doi.org/10.1021/acs.energyfuels.1c02721.
- Zhang, Z., Li, P., Yuan, Y., et al., 2020. Quantitative prediction of fractures in shale using the lithology combination index. Minerals 10, 569. https://doi.org/ 10.3390/min10060569.
- Zou, C., Yang, Z., Tao, S., et al., 2013. Continuous hydrocarbon accumulation over a large area as a distinguishing characteristic of unconventional petroleum: the Ordos Basin, North-Central China. Earth Sci. Rev. 126, 358—369. https://doi.org/10.1016/j.earscirev.2013.08.006.